ECCOMAS Congress 2016
VII European Congress on Computational Methods in Applied Sciences and Engineering
M. Papadrakakis, V. Papadopoulos, G. Stefanou, V. Plevris (eds.)
Crete Island, Greece, 5–10 June 2016

LARGE EDDY SIMULATION OF TURBULENT COMPRESSIBLE FLOWS USING THE CHARACTERISTIC BASED SPLIT SCHEME AND MESH ADAPTATION

Renato V. Linn[1] **and Armando M. Awruch**[2]

[1]Federal University of Rio Grande do Sul
99 Osvaldo Aranha Ave. 4th floor, 90035-190, Porto Alegre, RS, Brazil
e-mail: renatolinn@ufrgs.br

[2] Graduate Program in Civil Engineering (PPGEC/UFRGS)
99 Osvaldo Aranha Ave. 3rd floor, 90035-190, Porto Alegre, RS, Brazil
e-mail: amawruch@ufrgs.br

Keywords: Computational Fluid Dynamics, Compressible Flow, Large Eddy Simulation, Mesh Adaptation

Abstract. *The simulation of high-speed turbulent compressible flows using a numerical method of Large Eddy Simulation (LES) combined with the Characteristic-Based Split scheme (CBS) and anisotropic mesh adaptation is presented in this work. The CBS scheme is a unified approach for Computational Fluid Dynamics (CFD) with capability of covering a wide range of flow speeds and types with good stability and accuracy compared with other numerical schemes of the same order [1]. Although LES of incompressible flows combined with the CBS scheme has already been successfully addressed, the compressible extension is not yet covered, been the main contribution of this work. The CBS scheme is employed in a Finite Element Method (FEM) context for space and time discretization using unstructured meshes with adaptation [2], allowing the representation of complex geometries with accuracy. The anisotropic mesh adaptation is performed with mesh refinement, mesh coarsening and edge swapping procedures. A compressible dynamic Smagorinsky model is employed for the compressible LES model. The developed code is used to investigate a complex turbulent transonic flow around a circular cylinder in a two-dimensional approach. Several complex flow features such as lamda-shock-waves, viscous interactions and Von Kármán vortex sheet effects are correctly captured by the mesh adaptation strategy and the computed aerodynamic coefficients are close to the experimental reported values.*

1 INTRODUCTION

The simulation of high-speed turbulent compressible flows at transonic and supersonic speed ranges has several difficulties. For aerodynamic problems, the accurate capturing of the complex three-dimensional shock waves and flow features developed is a challenging task which is hard to accomplished without making use of a mesh adaptation methodology. The adequate mesh to be used in the simulation depends on the desired resolution, the numerical algorithm employed, the flow characteristics and the geometry, thus being hard to be a priori determined even for an expert in CFD. Furthermore, the large mesh resolution required to correctly evaluate the smallest scales present in flows of high Reynold number, typically present in such type of problems, is prohibitive. Such constraints are alleviated by making use of a turbulence modelling strategy such as the Large Eddy Simulation (LES) combined with mesh adaptation.

Large Eddy Simulation (LES) directly calculates the large and energetic vortical structures in turbulent flows, while modelling the smaller-scales eddies. Therefore, compared to Reynolds-Averaged Navier-Stokes (RANS) models, the advantage of LES are significant, being RANS effective only for steady simulations of fluid flows. The LES model is combined with the Characteristic-Based split Scheme (CBS) [1] in this work to simulate turbulent compressible flows. The CBS scheme can handle with flows with a wide range of velocities. The capabilities of using the CBS scheme to solve compressible turbulent flows has not been investigated yet and it is the main objective of this work.

Mesh adaptation is combined with the turbulent flow solver in order to achieve a high resolution solutions together with low computational cost. The main procedures for mesh adaptation used in this work are mesh refinement, mesh coarsening and edge swapping. Mesh adaptation is evaluated anisotropically by making use of a metric-based methodology using the concept of Riemannian space to analyse the error as a tensorial quantity [2].

The developed algorithm is used to investigate a complex transonic turbulent flow around a circular cylinder in a two-dimensional approach. Even for a two-dimensional investigation, the obtained results are quite promising. The evaluated aerodynamic coefficients, Strouhal number and the complex flow features are in good agreements with experimental results.

2 GOVERNING EQUATIONS

For an arbitrary function $\mathcal{F}\left(x_i,t\right)$, the filtered variable $\bar{\mathcal{F}}\left(x_i,t\right)$ in physical space is represented by the convolution product [3]:

$$\bar{\mathcal{F}}\left(x_i,t\right) = \int_{\Omega} G\left(x_i-\xi_i,\Delta\right)\mathcal{F}\left(\xi_i,t\right)d\xi_i \tag{1}$$

where x_i are the Cartesian coordinates $(i=1,2)$, t is the time variable, G is the filter kernel, Ω represents the flow domain and Δ is a measure of the filter width and is related to the computational mesh size. For compressible flows, the density weighted variable $\widetilde{\mathcal{F}}\left(x_i,t\right)$ is employed:

$$\widetilde{\mathcal{F}}\left(x_i,t\right) = \frac{\overline{\rho\mathcal{F}}}{\overline{\rho}} \tag{2}$$

and the resulting filtered compressible Navier-Stokes equations are:

$$\frac{\partial\overline{\rho}}{\partial t} + \frac{\partial}{\partial x_i}\left(\overline{\rho}\widetilde{u}_i\right) \tag{3}$$

$$\frac{\partial\left(\overline{\rho}\widetilde{u}_j\right)}{\partial t}+\frac{\partial}{\partial x_i}\left(\overline{\rho}\widetilde{u}_i\widetilde{u}_j\right)-\frac{\partial\widetilde{\tau}_{ij}}{\partial x_i}-\frac{\partial\tau_{ij}^{sgs}}{\partial x_i}+\frac{\partial\overline{p}}{\partial x_j}+\frac{\partial\left(\overline{\tau}_{ij}-\widetilde{\tau}_{ij}\right)}{\partial x_i}=0 \tag{4}$$

$$\frac{\partial\left(\overline{\rho}\widetilde{E}\right)}{\partial t}+\frac{\partial}{\partial x_i}\left(\overline{\rho}\widetilde{E}\widetilde{u}_i\right)-\frac{\partial}{\partial x_i}\left(\widetilde{k}\frac{\partial\widetilde{T}}{\partial x_i}\right)+\frac{\partial}{\partial x_i}\left(\overline{p}\widetilde{u}_i\right)-\frac{\partial}{\partial x_i}\left(\widetilde{\tau}_{ij}\widetilde{u}_j\right)-C_p\frac{\partial q_i^{sgs}}{\partial x_i}- \tag{5}$$
$$\frac{\partial}{\partial x_k}\left(\left[\overline{\tau}_{ik}-\widetilde{\tau}_{ik}\right]\widetilde{u}_i\right)-\frac{1}{2}\frac{\partial}{\partial x_i}\overline{\rho}\left(\widetilde{u_k u_k}u_i-\widetilde{u}_k\widetilde{u}_k\widetilde{u}_j-\tau_{kk}^{sgs}\widetilde{u}_i\right)+\frac{\partial}{\partial x_i}\left(\overline{k}\frac{\partial\overline{T}}{\partial x_i}-\widetilde{k}\frac{\partial\widetilde{T}}{\partial x_i}\right)=0$$

where $\overline{\rho}$ is the mean density, $\widetilde{u}_i$ are the filtered Cartesian components of the velocity, $\overline{p}$ is the mean pressure, $\widetilde{\tau}_{ij}$ and $\overline{\tau}_{ij}$ are the filtered and mean molecular viscous stress tensor, respectively, $\widetilde{E}$ is the filtered total energy, $\widetilde{T}$ is the filtered absolute temperature, $\widetilde{k}$ and $\overline{k}$ are the filtered and mean diffusion coefficient, respectively, C_p is the specific heat coefficient at constant pressure, τ_{ij}^{sgs} is the sub-grid scale stress tensor and q_i^{sgs} is the sub-grid turbulent heat flux. The filtered viscous stress tensor is approximated by:

$$\widetilde{\tau}_{ij}=\widetilde{\mu}\left[\left(\frac{\partial\widetilde{u}_i}{\partial x_j}+\frac{\partial\widetilde{u}_j}{\partial x_i}\right)-\frac{2}{3}\delta_{ij}\frac{\partial\widetilde{u}_k}{\partial x_k}\right] \tag{6}$$

where $\widetilde{\mu}$ is the molecular viscosity based on the Favre-filtered static temperature $\widetilde{T}$ and δ_{ij} is the Kronecker delta. The temperature dependence of the molecular velocity is evaluated through the Sutherland's relation [4]:

$$\widetilde{\mu}=\frac{1.45\widetilde{T}^{3/2}}{\widetilde{T}+110}\times 10^{-6} \tag{7}$$

where all variables are in the SI system and $\widetilde{T}$ is given in Kelvin. The closure of the conservative equations is done with the addition of the state equation of a perfect gas:

$$\overline{p}=\left(\gamma-1\right)\overline{\rho}\widetilde{e} \tag{8}$$

where $\gamma=C_p/C_v$ with C_v is the specific heat coefficient at constant volume and $\widetilde{e}$ is the filtered internal energy.

The sub-grid scale stress tensor and the sub-grid turbulent heat flux are defined as:

$$\tau_{ij}^{sgs}=\overline{\rho}\left(\widetilde{u_i u_j}-\widetilde{u}_i\widetilde{u}_j\right) \tag{9}$$

$$q_i^{sgs}=\overline{\rho}\left(\widetilde{Tu_j}-\widetilde{T}\widetilde{u}_j\right) \tag{10}$$

The terms $(\overline{\tau}_{ij}-\widetilde{\tau}_{ij})$, $\frac{\partial}{\partial x_i}\left(\overline{k}\frac{\partial\overline{T}}{\partial x_i}-\widetilde{k}\frac{\partial\widetilde{T}}{\partial x_i}\right)$ and $\frac{1}{2}\frac{\partial}{\partial x_i}\overline{\rho}\left(\widetilde{u_k u_k}u_i-\widetilde{u}_k\widetilde{u}_k\widetilde{u}_j-\tau_{kk}^{sgs}\widetilde{u}_i\right)$ are neglected due to its small contribution to the filtered conservation equations, following the results of [5, 6, 7, 8]. Finally, the total energy is approximated by [9, 10]:

$$\overline{\rho}\widetilde{E}=\overline{\rho}C_v\widetilde{T}+\frac{1}{2}\overline{\rho}\widetilde{u}_i\widetilde{u}_i+\frac{1}{2}\tau_{ii}^{sgs} \tag{11}$$

Based on the widely used sub-grid eddy viscosity model, the sub-grid stress tensor can be written as:

$$\tau_{ij}^{sgs} = 2\overline{\rho}\nu_{sgs}\left(\widetilde{S}_{ij} - \frac{1}{3}\widetilde{S}_{kk}\delta_{ij}\right) - \frac{1}{3}\tau_{kk}^{sgs}\delta_{ij} \tag{12}$$

where the rate of strain tensor $\widetilde{S}_{ij}$ is defined by:

$$\widetilde{S}_{ij} = \frac{1}{2}\left(\frac{\partial \widetilde{u}_i}{\partial x_j} + \frac{\partial \widetilde{u}_j}{\partial x_i}\right) \tag{13}$$

and the trace of sub-grid stress τ_{kk}^{sgs} tensor is modelled separately. The dynamic compressible Smagorinsky model is used in this work to evaluate the sub-grid viscosity ν_{sgs} and thus τ_{ij}^{sgs}, q_i^{sgs} and τ_{ii}^{sgs} [11].

The numerical solution of the flow equations is performed with the Characteristic-Based Split (CBS) scheme introduced by Zienkiewicz and Codina [12]. For the solution of the governing equations, the CBS algorithm uses a fractional step with a split. The four steps can be briefly described as [13]:

1. solve momentum equation without pressure terms,
2. calculate pressure solving a Poisson equation,
3. correct velocity components,
4. calculate additional scalar variables, such as temperature, from appropriate governing equations.

The time increment is assumed to be $\Delta t = t^{n+1} - t^n$ and the flux mass $U_i^{n+1} = \rho u_i$, evaluated at time $n+1$, is split into two terms:

$$U_i^{n+1} = U_i^n + \Delta U_i^* + \Delta U_i^{**} \tag{14}$$

A standard Galerkin finite element procedure is used for spatial discretization. Linear triangular and elements are employed in the present work. The spatial discretization of the variables is carried out as:

$$\begin{array}{llll} U_i = \mathbf{N}_u\widehat{\mathbf{U}}_i, & \Delta U_i = \mathbf{N}_u\Delta\widehat{\mathbf{U}}_i, & \Delta U_i^* = \mathbf{N}_u\Delta\widehat{\mathbf{U}}_i^*, & \Delta U_i^{**} = \mathbf{N}_u\Delta\widehat{\mathbf{U}}_i^{**} \\ u_i = \mathbf{N}_u\widehat{\mathbf{u}}_i, & p = \mathbf{N}_p\widehat{\mathbf{p}}, & \rho = \mathbf{N}_\rho\widehat{\rho} & \end{array} \tag{15}$$

where a hat superscript represents a nodal quantity and $\mathbf{N}_i$ are the shape functions such that:

$$\widehat{\mathbf{U}}_i = \left[U_i^1, U_i^2, \cdots, U_i^a, \cdots, U_i^m\right]^T \tag{16}$$

$$\mathbf{N}_j = \left[N_j^1, N_j^2, \cdots, N_j^a, \cdots, N_j^m\right] \tag{17}$$

with a being a node (or variable), which varies from 1 to m, $i = 1, p$ and $j = u_i, p, \rho$.

The semi-discrete forms of the CBS equations are then weighted by $\mathbf{N}^T$ and integrated over the domain. The final equations for the four steps of the CBS scheme for the explicit formulation is summarized as:

- Step 1, obtain $\Delta\tilde{\mathbf{U}}_i^*$:

$$\mathbf{M}\Delta\widehat{\mathbf{U}}_i^* = \Delta t\Big[(\mathbf{C}-\mathbf{S})\left(\widehat{\mathbf{u}}_j\widehat{\mathbf{U}}_i\right) - (\mathbf{K}_\tau - \mathbf{T}_\tau)\,\mathcal{T}_{ij}\Big]^n - \frac{\Delta t^2}{2}\widehat{\mathbf{u}}_k\Big[(\mathbf{K}_u - \mathbf{T}_u)\left(\widehat{\mathbf{u}}_j\widehat{\mathbf{U}}_i\right) + (\mathbf{K}_p - \mathbf{T}_p)\,\widehat{\mathbf{p}}\Big]^n \tag{18}$$

- Step 2, obtain $\Delta\tilde{\rho}$:

$$\mathbf{M}\Delta\widehat{\rho} = \Delta t\Big[(\mathbf{D}-\mathbf{R}_u)\left(\widehat{\mathbf{U}}_i + \theta_1\Delta\widehat{\mathbf{U}}_i^*\right) - \Delta t\theta_1\mathbf{K}\widehat{\mathbf{p}}\Big]^n \tag{19}$$

- Step 3, obtain $\tilde{\mathbf{U}}_i$, thus establishing the values at t^{n+1}:

$$\mathbf{M}\widehat{\mathbf{U}}_i = \mathbf{M}\Delta\widehat{\mathbf{U}}_i^* + \Delta t[(\mathbf{D}-\mathbf{R}_u)\,\widehat{\mathbf{p}}]^n \tag{20}$$

- Step 4, solve energy equation to obtain the value $\Delta\tilde{\rho}\tilde{\mathbf{E}}$:

$$\mathbf{M}\Delta\widehat{\rho}\widehat{\mathbf{E}} = \Delta t\Big[(\mathbf{C}-\mathbf{S})\,\widehat{\mathbf{u}}_j\left(\widehat{\rho}\widehat{\mathbf{E}} + \widehat{\mathbf{p}}\right) - (\mathbf{T}_\tau - \mathbf{K}_\tau)\left(\mathcal{Q}_i + \mathcal{T}_{ij}\widehat{\mathbf{u}}_j\right)\Big]^n - \frac{\Delta t^2}{2}\Big[\widehat{\mathbf{u}}_k\,(\mathbf{K}_u - \mathbf{T}_u)\,\widehat{\mathbf{u}}_j\left(\widehat{\rho}\widehat{\mathbf{E}} + \widehat{\mathbf{p}}\right)\Big]^n \tag{21}$$

where $\mathcal{T}_{ij} = \tau_{ij} + \tau_{ij}^{sgs}$ is the total stress, $\mathcal{Q}_i = k\frac{\partial T}{\partial x_i} + q_i^{sgs}$ is the total heat flux and the vector and matrices are given by:

$$\mathbf{M} = \int_\Omega \mathbf{N}^T\mathbf{N}d\Omega \qquad \mathbf{R}_u = \int_\Omega \mathbf{N}^T\mathbf{N}n_i d\Omega \qquad \mathbf{S} = \int_\Gamma \mathbf{N}^T\mathbf{N}n_j d\Gamma \tag{22a}$$

$$\mathbf{C} = \int_\Omega \frac{\partial\mathbf{N}^T}{\partial x_j}\mathbf{N}d\Omega \qquad \mathbf{D} = \int_\Omega \frac{\partial\mathbf{N}^T}{\partial x_i}\mathbf{N}d\Omega \qquad \mathbf{K} = \int_\Omega \frac{\partial\mathbf{N}^T}{\partial x_i}\frac{\partial\mathbf{N}}{\partial x_i}d\Omega \tag{22b}$$

$$\mathbf{K}_\tau = \int_\Omega \frac{\partial\mathbf{N}^T}{\partial x_j}d\Omega \qquad \mathbf{K}_u = \int_\Omega \frac{\partial\mathbf{N}^T}{\partial x_k}\frac{\partial\mathbf{N}}{\partial x_j}d\Omega \qquad \mathbf{K}_p = \int_\Omega \frac{\partial\mathbf{N}^T}{\partial x_k}\frac{\partial\mathbf{N}}{\partial x_i}d\Omega \tag{22c}$$

$$\mathbf{T}_\tau = \int_\Gamma \mathbf{N}^T n_j d\Gamma \qquad \mathbf{T}_u = \int_\Gamma \mathbf{N}^T\frac{\partial\mathbf{N}}{\partial x_j}n_k d\Gamma \qquad \mathbf{T}_p = \int_\Gamma \mathbf{N}^T\frac{\partial\mathbf{N}}{\partial x_i}n_k d\Gamma \tag{22d}$$

with $\theta_1 = 0.5$ for a second-order accuracy (Crank-Nicolson scheme) in time for the velocity.

For transonic and supersonic speeds, an additional shock capturing dissipation is introduced to capture and smooth local oscillations in the vicinity of shocks. A method based on the Hessian of pressure is employed, modifying $\widehat{\mathbf{\Phi}}^{n+1} = \left\{\widehat{\rho}, \widehat{u}_i, \widehat{E}\right\}$ evaluated in time $n+1$ to $\widehat{\mathbf{\Phi}}_s^{n+1}$ by [14]:

$$\widehat{\mathbf{\Phi}}_s^{n+1} = \widehat{\mathbf{\Phi}}^{n+1} - \Delta t\mathbf{M}_L^{-1}C_e h^3\frac{|\mathbf{u}|+c}{p}\left|\frac{\partial^2 p}{\partial x_i^2}\right|_e^n\left(\int_\Omega \frac{\partial\mathbf{N}^T}{\partial x_i}\frac{\partial\mathbf{N}}{\partial x_i}d\Omega\right)\widehat{\mathbf{\Phi}}^n \tag{23}$$

where h is the element size [14], c is the local sound speed, C_e is an user-informed constant and the subscript e represents an element [1].

The following local time stepping is employed [13]:

$$\Delta t = \min\left(\frac{h}{c+|\mathbf{u}|}, \frac{h^2}{2\nu}\right)\theta_c \tag{24}$$

where θ_c is an user specified number between 0 and 1 used to not violate the Courant-Friedrichs-Lewy condition.

3 MESH ADAPTATION

Both the direction and the magnitude of the anisotropy are important and necessary information required for the construction of an anisotropic mesh adaptation procedure. These information can be evaluated through the use of the so called metric-based methods, where a Riemannian metric space is evaluated based on the interpolation error of the solution field. The most important features of the metric-based method employed in this work for two-dimensional problems is briefly described in this section. A more detailed overview of such methodology can be found in references [15, 2].

3.1 Metric Estimates

The length $\ell_{\mathcal{M}}(\mathbf{ab})$ of an edge $\mathbf{ab}$ can be continuously evaluated in a Riemannian metric space with a parametrization given by $\gamma(t) = \mathbf{a} + t\mathbf{ab}$ with $t \in [0, 1]$ as:

$$\ell_{\mathcal{M}}(\mathbf{ab}) = \int_0^1 \|\gamma'(t)\|_{\mathcal{M}} dt = \int_0^1 \sqrt{\mathbf{ab}^T \mathcal{M}(\mathbf{a} + t\,\mathbf{ab})\,\mathbf{ab}}\, dt \tag{25}$$

where $\mathcal{M}$ is a 2×2 symmetric positive definite matrix called metric tensor, or just metric. The size $|T_K|_{\mathcal{M}}$ of an element K evaluated in the Riemannian metric space is determined by:

$$|T_K|_{\mathcal{M}} = \int_K \sqrt{\det \mathcal{M}(\mathbf{x})} d\mathbf{x} \tag{26}$$

The anisotropic quality of an element K can be monitored through a quality function $Q_{\mathcal{M}}$ that combines both sizing and orientation information [16]:

$$Q_{\mathcal{M}}(K) = \frac{\sum \ell^2_{\mathcal{M}}(A_K)}{|T_K|_{\mathcal{M}}} \tag{27}$$

where A_K are the edges of an element K. In the previous equation, the numerator takes into account the sizing of the mesh. Decreasing the length of the edges evaluated in the Riemannian space also reduces $Q_{\mathcal{M}}$. The denominator is a measure of the orientation of the simplex in the Riemannian space, where a simplex oriented closer to the local field eigenvectors leads to a reduction of $Q_{\mathcal{M}}$. Thus, minimizing $Q_{\mathcal{M}}$ the quality of the element becomes maximized in an anisotropic sense.

From a discrete point of view, the metric field need to be interpolated to evaluate approximate length and volume in the Riemannian space. Considering a linear interpolation of the metric tensor, the integration of Eq. 25 is evaluated by [17]:

$$\ell_{\mathcal{M}}(\mathbf{ab}) \approx \frac{2}{3} \frac{\ell_0^2 + \ell_0 \ell_1 + \ell_1^2}{\ell_0 + \ell_1} \tag{28}$$

where $\ell_i(\mathbf{ab}) = \sqrt{\mathbf{ab}^T \mathcal{M}(\mathbf{x}_i) \mathbf{ab}}$ is the length of the edge in metric $\mathcal{M}(\mathbf{x}_i)$ with $i = 1, 2$ for the edge end-points $\mathbf{a}$ and $\mathbf{b}$, respectively. Similarly, the integral of Eq. 26 can be numerically approximated by:

$$|T_K|_{\mathcal{M}} \approx \sqrt{\det \frac{1}{3} \sum_{i=1}^{3} \mathcal{M}_i(\mathbf{x})}\, |T_K| \tag{29}$$

where $\mathcal{M}_i(\mathbf{x})$ is the metric at each of the i vertices of the element K (assumed as a triangle) with Euclidean oriented measure $|T_K|$.

The error $E_{\mathbf{L}^p}(\mathbf{ab})$ estimated for an edge $\mathbf{ab}$ is defined as the upper bound of the difference between a quadratic approximation and the evaluated linear interpolation measured in the $\mathbf{L}^p$ norm for a given continuous function ϕ, which can be expressed as:

$$E_{\mathbf{L}^p}(\mathbf{ab}) \equiv \ell_{\mathcal{M}}\left(\mathbf{ab}\right) \tag{30}$$

with the metric $\mathcal{M}\left(\mathbf{x}\right)$ defined as the normalized Hessian of the function ϕ measured in the $\mathbf{L}^p$ norm [18]:

$$\mathcal{M}\left(\mathbf{x}\right) = \mathcal{M}_{\mathbf{L}^p}\left(\mathbf{x}\right) = \left(\det\left|\mathbf{H}\right|\right)^{-\frac{1}{2p+d}}\left|\mathbf{H}\right| \tag{31}$$

where $\mathbf{H}$ is a symmetric matrix representing the Hessian of ϕ. As $\mathbf{H}$ is a symmetric matrix, it can be decomposed into the product of orthonormal matrices $\mathcal{R}$ of associated eigenvectors and a diagonal matrix $\mathbf{\Lambda}$ of eigenvalues. To ensure that $\mathbf{H}$ is a positive-defined matrix and limited, $\left|\mathbf{H}\right| = \mathcal{R}\left|\tilde{\mathbf{\Lambda}}\right|\mathcal{R}^T$ is obtained as the Hessian matrix with normalized and limited eigenvalues $\tilde{\lambda}_i$ of $\tilde{\mathbf{\Lambda}} = \text{diag}\left(\tilde{\lambda}_i\right)$ such that [15]:

$$\tilde{\lambda}_i = \min\left(\max\left(\lambda_i, \frac{1}{h^2_{\max}}\right), \frac{1}{h^2_{\min}}\right) \tag{32}$$

with $h_{\max}$ and $h_{\min}$ as the maximum and minimum allowed edge size in the mesh and the Hessian matrix is evaluated by a double projection scheme using a weak formulation [19].

3.2 Metric Intersection

When more than one metric is simultaneously specified at one point, the resulted metric should cover the minimum error associated to each of these metrics. Therefore, a metric intersection procedure is used in this work. A common basis $\mathcal{P}$ of two metrics $\mathcal{M}_A$ and $\mathcal{M}_B$ is looked for, such that they are congruent to a diagonal matrix at its basis. The matrix $\mathcal{B} = {\mathcal{M}_A}^{-1}\mathcal{M}_B$ is introduced, such that $\mathcal{B}$ is diagonalizable with real eigenvalues. The normalized eigenvectors of $\mathcal{B}$ are $\mathbf{e}_i$ with $i = 1, 2$ and compose the common diagonalizable basis $\mathcal{P}$. The principal components of $\mathcal{M}_A$ and $\mathcal{M}_B$ projected in this basis can be obtained with [15]:

$$\mu_i = \mathbf{e}_i^T\mathcal{M}_A\mathbf{e}_i \quad \text{and} \quad \beta_i = \mathbf{e}_i^T\mathcal{M}_B\mathbf{e}_i \tag{33}$$

As $\mathcal{P}$ is also invertible, the metric intersection can be evaluated through:

$$\mathcal{M}_{A\cap B} = \mathcal{M}_A \cap M_B = \left(\mathcal{P}^{-1}\right)^T\text{diag}\left(\max\left(\mu_i, \beta_i\right)\right)\mathcal{P}^{-1} \tag{34}$$

For a third metric $\mathcal{M}_C$ to be intersected, the same procedure is performed, with $\mathcal{M}_{AB\cap C}$ employing $\mathcal{M}_{AB} = \mathcal{M}_{A\cap B}$ and so on for more metric intersections.

3.3 Mesh Refinement, Mesh Coarsening and Edge Swapping

The present mesh adaptation procedure uses the metric-based framework to evaluate the error associated to each edge of the mesh. When the error is above a specified value, the edge is split into two new edges. When the error is less than the desired, the edge is removed by an edge collapse procedure. Edge and face swapping are also used to improve the mesh quality.

When an edge $\mathbf{ab}$ is refined, a new node $\mathbf{c}$ is inserted generating two new edges: $\mathbf{ac}$ and $\mathbf{cb}$. A Riemannian centred is used, such that the new inserted node $\mathbf{c}$ verifies the following relation:

$$\ell_{\mathcal{M}}\left(\mathbf{ac}\right) = \ell_{\mathcal{M}}\left(\mathbf{cb}\right) \tag{35}$$

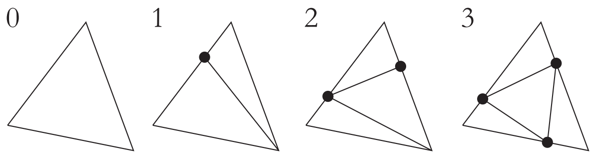

Figure 1: Edge-based anisotropic triangular subdivision scheme.

The spatial variation of the metric must be taken into account to solve the non-linear integral relation defined by Eq. 35. Moreover, using Eq. 25 and the parametrization $\mathbf{ac} = m\mathbf{ab}$ and $\mathbf{cb} = (1-m)\,\mathbf{ab}$ with $m \in [0,1]$, the Riemannian centred split defined in Eq. 35 can be evaluated by finding m such that:

$$\int_0^1 \sqrt{\mathbf{ac}^T \mathcal{M}\left(\mathbf{a} + t\,\mathbf{ac}\right)\mathbf{ac}}\,dt = \int_0^1 \sqrt{\mathbf{cb}^T \mathcal{M}\left(\mathbf{c} + t\,\mathbf{cb}\right)\mathbf{cb}}\,dt \tag{36}$$

and considering a linear interpolation of the metric tensor along $\mathbf{ab}$, the value of m is obtained as:

$$m = \frac{\ell_0^2 - 2^{-\frac{2}{3}}(\ell_0^3 + \ell_1^3)^{\frac{2}{3}}}{\ell_0^2 - \ell_1^2} \tag{37}$$

valid for all values of ℓ_0 and ℓ_1 such that $\ell_0 \neq \ell_1$. If $\ell_0 = \ell_1$, there is no size gradation and the Euclidean center is chosen for the split, with $m = 1/2$.

The refinement procedure must ensure that the topology of the mesh will not be violated, generating only valid elements. In order to satisfy this condition, the partitioning of an element is performed according to the number and position of the refined edges. All anisotropic partitioning cases are covered. For a mesh composed by triangular elements, four types of subdivision are possible, covering eight anisotropic cases (see Fig. 1). This type of edge subdivision is unique and can always be performed (existence and uniqueness conditions are satisfied), ensuring that the topology will not be violated.

An edge is coarsened by an edge collapse procedure. Let $\mathbf{ab}$ be an edge to be coarsened, with initial vertex $\mathbf{a}$ and final vertex $\mathbf{b}$. The vertices $\mathbf{a}$ and $\mathbf{b}$ are joined along the direction of the edge $\mathbf{ab}$ to a new point $\mathbf{c}$ between $\mathbf{a}$ and $\mathbf{b}$, collapsing all elements that share at least one edge with $\mathbf{ab}$. To hold the anisotropic information along the procedure, the choice of the collapsed point $\mathbf{c} = \mathbf{a} + n\mathbf{ab}$ is performed by finding $n \in [0,1]$ that minimizes the sum of all quality functions of the remaining elements affected by the collapse:

$$\min_{n\in[0,1]} \sum_{K\in B} Q_{\mathcal{M}}\left(K\right) \tag{38}$$

subjected to the following constraints:

$$|T_K| \;\forall\, K \in B > 0 \tag{39a}$$

$$\sum_{K\in A} |T_K| - \sum_{K\in B} |T_K| = 0 \tag{39b}$$

where B is the remaining set of elements affected by the procedure after the collapse and A the original set (see Fig. 2). A discrete approach is employed to solve Eq. 38 in this work. The continuous parametrization n is replaced by $n_c \geq 2$ discrete positions $n_j \in [0,1]$:

$$n_j = \frac{(j-1)}{(n_c - 1)} \tag{40}$$

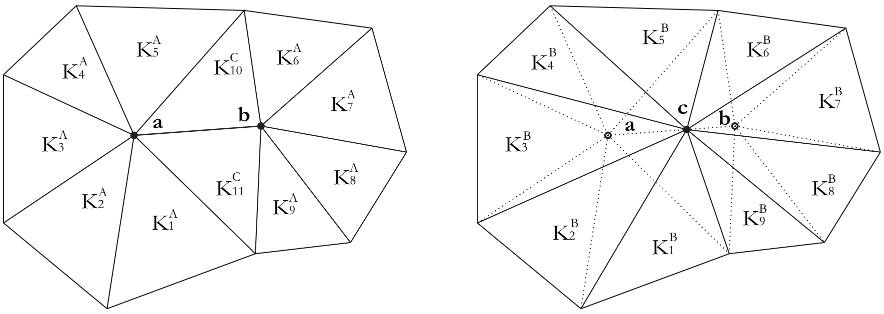

Figure 2: Edge collapse procedure.

with $j = 1, \ldots, n_c$. For each n_j position, the summation of Eq. 38 is evaluated using Eq. 27 and considering a linear interpolation of the metric tensor between $\mathbf{a}$ and $\mathbf{b}$. Finally, the position n_j which has the minimum value for this objective function and that does not violate the constraints of Eqs. 39 is chosen as the collapse point. This discrete approach is equivalent to choose between collapse the edge to one of the edge endpoints $\mathbf{a}$ or $\mathbf{b}$ if $n_c = 2$. For $n_c = 3$, the Euclidean midpoint is also considered as a possible position for the collapse and so on. In this work, $n_c = 10$ is adopted, allowing several possibilities for the choice of the position of point $\mathbf{c}$.

Edge swapping is performed in order to increase the mesh quality by alternating the edge connectivities. An edge $\mathbf{ab}$ that does not lye in the boundary of the domain shares two neighbour elements: K_1 and K_2. The internal edge of such elements can be swapped in order to obtain the elements K_1' and K_2' (see Fig. 3). The following condition is verified:

$$\max\left\{Q_{\mathcal{M}}\left(K'_1\right), Q_{\mathcal{M}}\left(K'_2\right)\right\} < \max\left\{Q_{\mathcal{M}}\left(K_1\right), Q_{\mathcal{M}}\left(K_2\right)\right\} \tag{41}$$

If such condition holds and no degenerated elements are obtained, then the swapping is performed, increasing the anisotropic quality of the mesh.

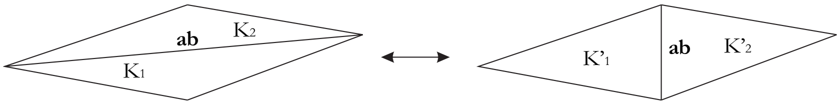

Figure 3: Edge swapping procedure.

3.4 Adaptation Algorithm

The overall algorithm implemented in this work performs the following sequence of local mesh modifications:

1. Refine edges with error above a given error threshold value η_U;
2. Edge swapping until convergence;
3. Coarse edges with error below a given error threshold value η_L;
4. Edge swapping until convergence.

which defines one adaptation iteration. An edge $\mathbf{ab}$ is refined if $E_{\mathbf{L}^p}(\mathbf{ab}) \geq \eta_U \varepsilon_{\mathbf{L}^p}$ and it is coarsened if $E_{\mathbf{L}^p}(\mathbf{ab}) \leq \eta_L \varepsilon_{\mathbf{L}^p}$, where $\varepsilon_{\mathbf{L}^p}$ is the target adaptation error measured in the

$\mathbf{L}^p$ norm. The upper and lower error threshold values η_U and η_L are assumed as 1.4 and 0.6, respectively [17]. As the investigated flows are compressible and turbulent, the continuous function u chosen for the adaptation is the intersection of all conservative flow field variables, with $\phi = \rho \cap u_i \cap E$ for the error estimation in Eq. 31 and the adaptation is performed at each t_a iterations of flow solver.

4 Test Case: Turbulent Transonic Flow Around a Circular Cylinder

The studied test case consists of a turbulent transonic flow around a circular cylinder. The circular cylinder has a diameter of $D = 1$ with center located at coordinates $x = 0$, $y = 0$. The domain Ω is circular with radius $R = 25D$. The free stream Mach number employed is $M_\infty = 0.80$ and the free stream Reynolds number is $Re_\infty = 500.000$. The simulation is carried from the initial time set to zero to the final time $T = 50s$. Mesh adaptation is performed at each ten iterations of flow solver ($t_a = 10$) in order to control a target interpolation error of $\varepsilon_{\mathbf{L}^p} = 0.05$ measured in the $\mathbf{L}^2$ norm. The maximum and the minimum allowed edge sizes are $h_{\max} = 1D$ and $h_{\min} = 0.003D$, respectively.

Fig. 4 and Fig. 5 show the gradient magnitude of the mass density and the corresponding mesh at two different instants. In these figures, the complexity of the developed flow around the cylinder, involving complex viscous interactions with shock waves together with the high transient nature of such effects is evident. The separation point of the boundary layer is associated with the formation of lambda-shock-waves of different sizes and intensities. There is also the formation shock-waves linking and interacting with vortices rotating in opposite directions. Finally, there is the formation of a Von Kármán vortex sheet after a zone of intense interaction of viscous and shock-wave effects.

Fig. 6 and Fig. 7 show the unsteady lift C_l and drag C_d coefficients, respectively. The average drag coefficient obtained in the present work is $C_d = 1.61$ while the reference [20] experimental value is $C_d = 1.50$. The power spectra P_l of the lift coefficient as function of the Strouhal number St is shown in Fig. 8, where a pronounced pic close to the value of $St = 0.18$ is present. The experimental value for this pic response reported by [20] is also the exact same value. Finally, the power spectra P_d of the drag coefficient as function of the Strouhal number St is shown in Fig. 9. In this case, there is not only one pronounced pic.

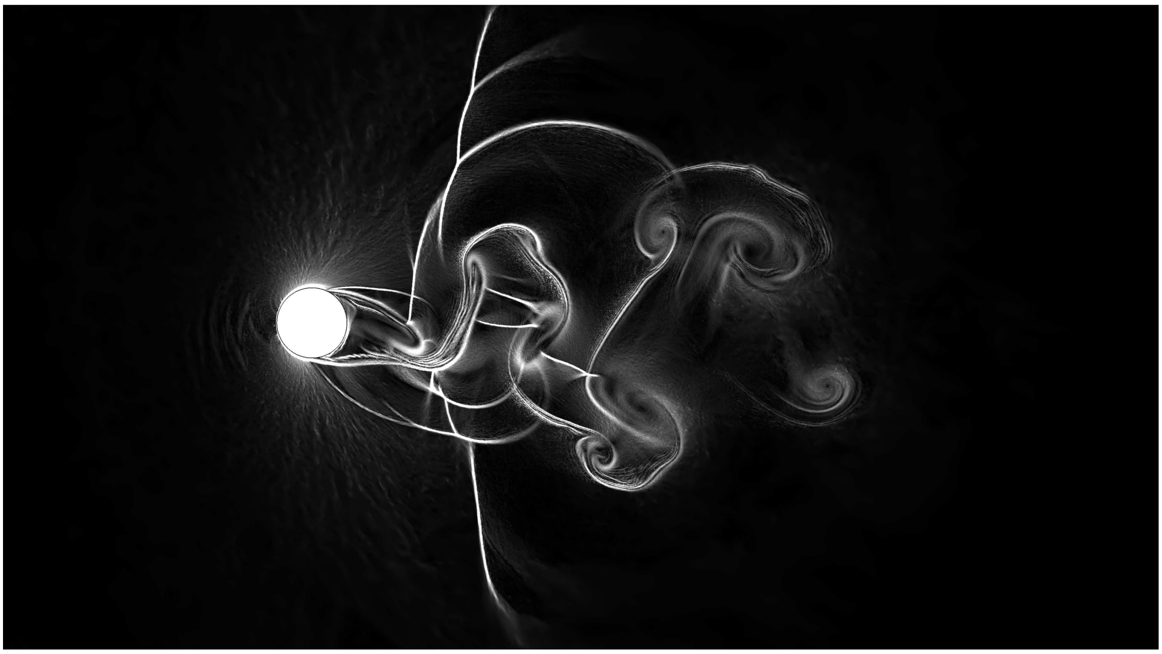

(a) Gradient magnitude of density. Scale: black (zero) to white (three).

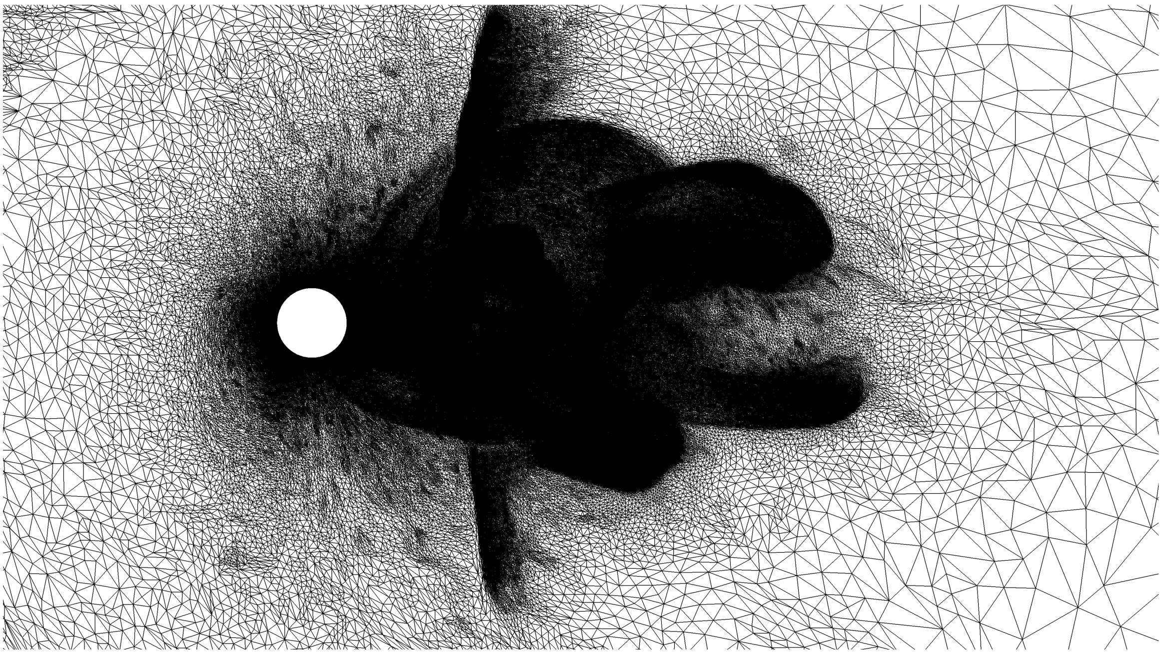

(b) Mesh

Figure 4: Flow field and mesh at time $t = 20s$.

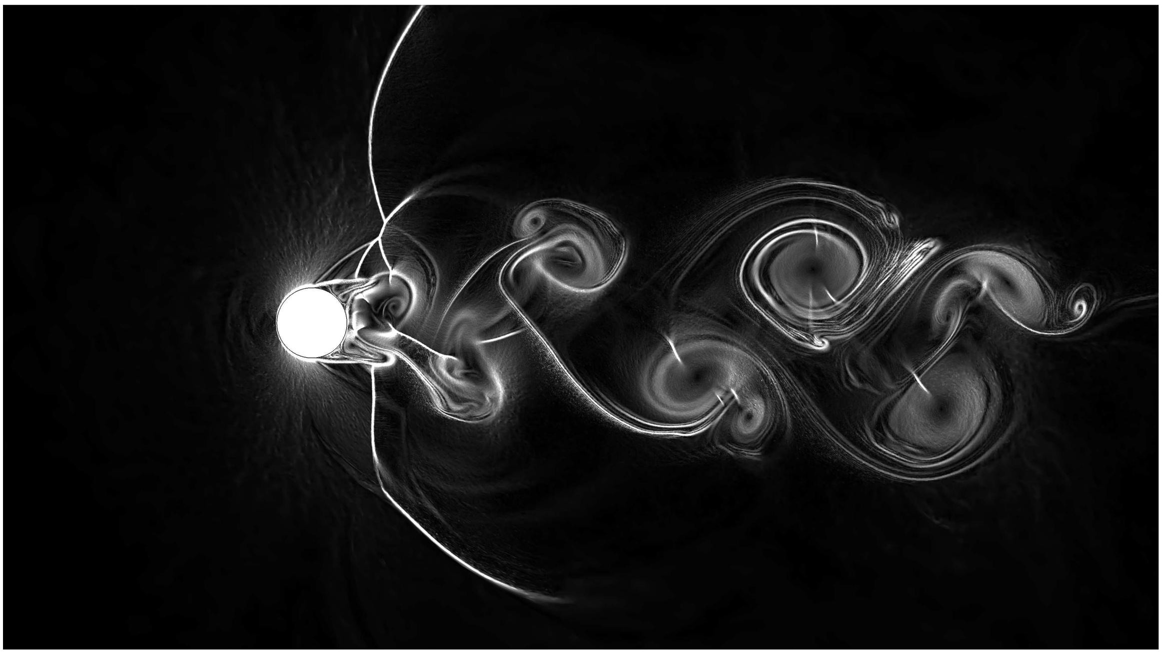

(a) Gradient magnitude of density. Scale: black (zero) to white (three).

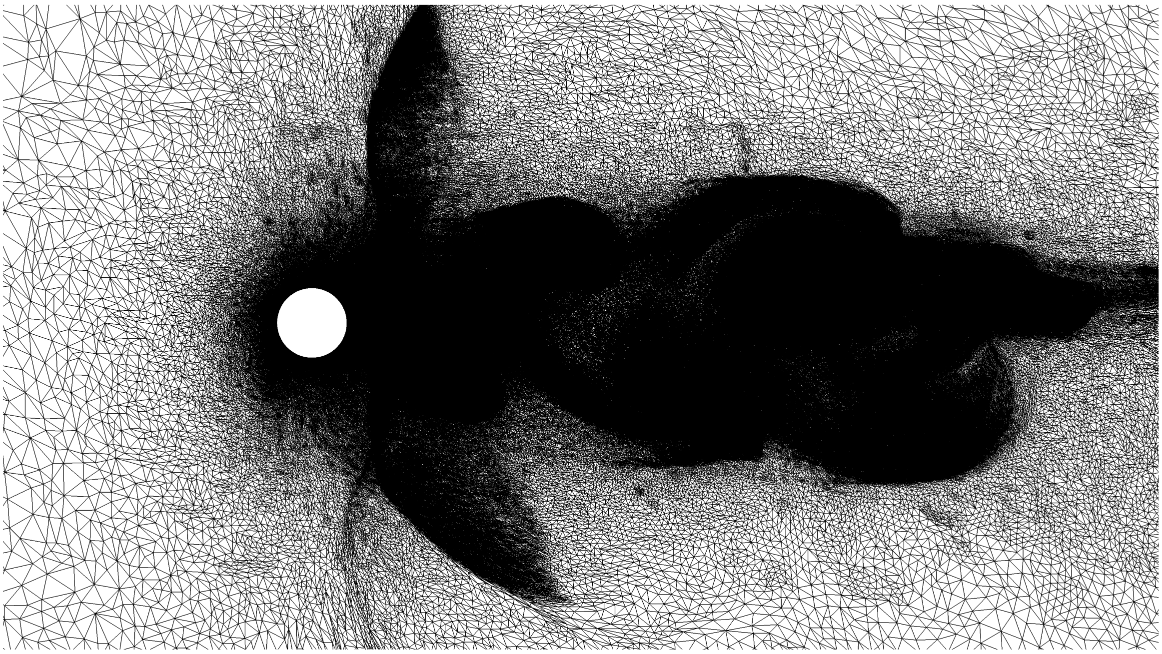

(b) Mesh

Figure 5: Flow field and mesh at time $t = 25s$.

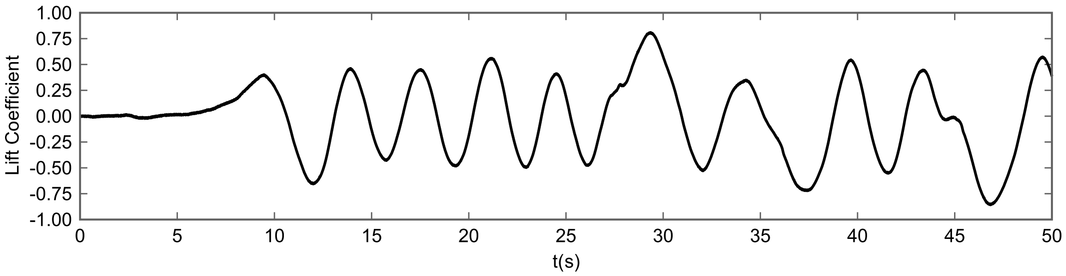

Figure 6: Unsteady lift coefficient.

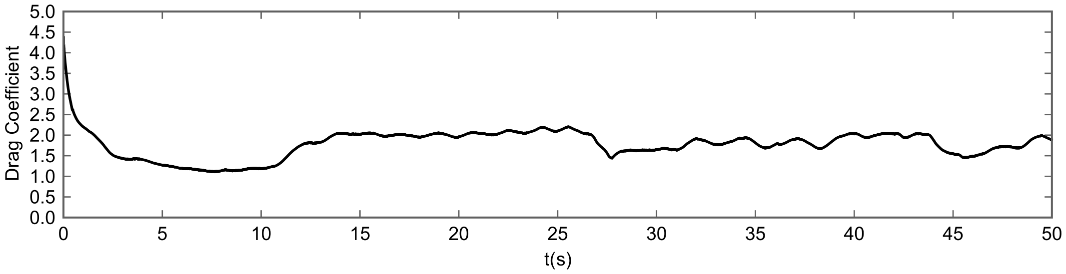

Figure 7: Unsteady drag coefficient.

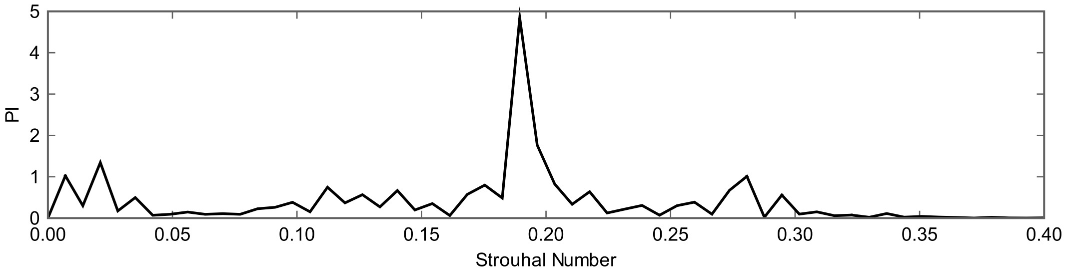

Figure 8: Power spectra of lift coefficient.

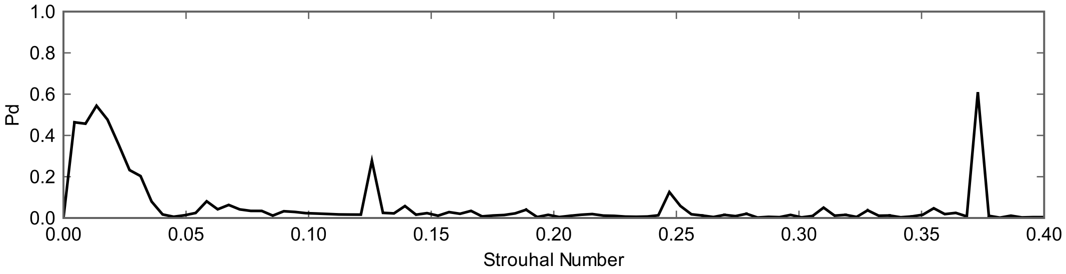

Figure 9: Power spectra of drag coefficient.

5 CONCLUSIONS

The coupling of the CBS algorithm with a dynamic Smagorinsky model for simulating turbulent compressible flows and anisotropic mesh adaptation is presented in this work. The developed code is used to investigate a complex turbulent transonic flow around a circular cylinder in a two-dimensional approach. The complex lamda-shock-waves, viscous interactions and Von Kármán vortex sheet effects are correctly captured by the mesh adaptation strategy, and the computed aerodynamic coefficients are in excellent agreement with the experimental reported values, even for a two-dimensional model. Although these preliminaries results are promising, an extension of the proposed methodology to a three-dimensional case is the next required step for validation of the computations.

Acknowledgements

The authors wish to thank to Propesq–UFRGS, CAPES and CNPq (Brazilian Research Committees) for their financial support and they thank also to CESUP (UFRGS Supercomputing Center) for its important contributions.

REFERENCES

[1] P. Nithiarasu, R. Codina O.C. Zienkiewicz, The Characteristic-Based Split (CBS) scheme– a unifief approach to fluid dynamics. *International Journal for Numerical Methods in Engineering*, **66**,1514–1546, 2006.

[2] M. J. Castro-Diaz, F. Hiecht, B. Mohammadi, O. Pironneau, Anisotropic unstructured mesh adaptation for flow simulation. *International Journal for Numerical Methods in Fluids*, **25**,475–491, 1997.

[3] D. Knight, G. Zhou, N. Okong's, V. Shukla, Large Eddy Simulation of Compressible Flows Using Unstructured Grids. *International Journal of Computational Fluid Dynamics*, **13**,303–326, 2000.

[4] C. Hirsch, *Numerical Computation of Internal and External Flows, Vol 1, Fundamentals of Numerical Discretization*. Wiley, 1988.

[5] M.P. Martin, U. Piomelli, G. Candler, Sub-Grid Scale for Compressible Large Eddy Simulations. *Theoretical Computational Fluid Dynamics* **13**,361–376, 2000.

[6] S. Santhanam, S.K. Lele, J.H. Ferzinger, A Robust High-Order Compact Method for Large-Eddy Simulation. *Journal of Computational Physics* **191**,392–419, 2003.

[7] B. Vreman, B. Geurts, H. Kuerten, A Priori Tests of Large Eddy Simulation of the Compressible Plane Mixing Layer. *Journal of Engineering Mathematics*, **29**,299–327, 1995.

[8] B. Vreman, B. Geurts, H. Kuerten, Subgrid-Modeling in LES of Compressible Flow. *Applied Science Research* **54**,191–203, 1995.

[9] B. Kosovic, D.I. Pullin, R. Samtaney, Subgrid-Scale Modeling for Large Eddy Simulation of Compressible Turbulence. *Phys. Fluids*, **14**,1511–1522, 2002.

[10] T. Dubois, J.A. Domaradzki, A. Honein, The Subgrid Scale Estimation Model Applied to Large Eddy Simulations of Compressible Turbulence. *Physics of Fluids*, **14**,1781–1801, 2002.

[11] P. Moin, K. Squires, W. Cabot, S. Lee, A Dynamic Subgrid-Scale Model for Compressible Turbulence and Scalar Transport. *Physics of Fluids A* **11**,2746–2757, 1991.

[12] O.C. Zienkiewicz, R. Codina, A general algorithm for compressible and incompressible flow – part I: The split, characteristic-based scheme. *International Journal for Numerical Methods in Fluids*, **20**,869–885, 1995.

[13] O.C. Zienkiewicz, R.L. Taylor, P. Nithiarasu, *The Finite Element Method for Fluid Dynamics, 6th Edition*. Elseliver, 2005.

[14] P. Nithiarasu, O.C. Zienkiewicz, B.V.K. Satya-Sai, K. Morgan, M. Vázquez, Shock capturing viscosities for the general fluid mechanics algorithm. *International Journal for Numerical Methods in Fluids*, **28**,1325–1353, 1998.

[15] P. J. Frey, F. Alauzet, Anisotropic mesh adaptation for CFD computations. *Computer Methods in Applied Mechanics and Engineering*, **194**,5068–5082, 2005.

[16] C. Alexandra, V. Ducrot, Levelsets and anisotropic mesh adaptation. *Discrete and Continuous Dynamical Systems*, **30**,165–183, 2009.

[17] W. G. Habashi, J. Dompierre, Y. Bourgault, D. Ait-Ali-Yahia, M. Fortin, M. G. Vallet, Anisotropic Mesh Adaptation: Towards User-Independent, Mesh-Independent and Solver Independent CFD. Part I: General Principles. *International Journal for Numerical Methods in Fluids*, **32**,725–744, 2000.

[18] F. Alauzet, A changing-topology moving mesh technique for large displacements. *Engineering With Computers*, **30**,175–200, 2014.

[19] M. G. Vallet, C. -M. Manole, J. Dompierre, S. Dufour, F. Guibault, Numerical Comparison of some Hessian Recovery Techniques. *International Journal for Numerical Methods in Engineering*, **8**,987–1007, 2007.

[20] W.S. Murthy, C. Rose, From Drag, Skin Friction and Vortex Shedding Frequencies for Subsonic and Transonic Cross Flows on Circular Cylinder. *10th AIAA Fluid and Plasmodynamics Conference*, Albuquerque, NM, June 27-29, 1977.